

Baryon Acoustic Oscillations from the C IV Forest with DESI DR2

ABBY BAULT,¹ ANDREI CUCEU,^{1,2} JULIEN GUY,¹ J. AGUILAR,¹ S. AHLEN,³ D. BIANCHI,^{4,5} A. BRODZELLER,¹ D. BROOKS,⁶ R. CANNING,⁷ E. CHAUSSIDON,¹ T. CLAYBAUGH,¹ R. DE BELSUNCE,¹ A. DE LA MACORRA,⁸ ARJUN DEY,⁹ P. DOEL,⁶ S. FERRARO,^{1,10} A. FONT-RIBERA,^{11,12} J. E. FORERO-ROMERO,^{13,14} E. GAZTAÑAGA,^{15,7,16} S. GONTCHO A GONTCHO,^{1,17} C. GORDON,⁶ D. GREEN,¹ G. GUTIERREZ,¹⁸ C. HAHN,¹⁹ H. K. HERRERA-ALCANTAR,^{20,21} K. HONSCHIED,^{22,23,24} M. ISHAK,²⁵ R. JOYCE,⁹ S. JUNEAU,⁹ D. KIRKBY,²⁶ A. KREMIN,¹ C. LAMMAN,²⁴ M. LANDRIAUX,¹ L. LE GUILLOU,²⁷ M. E. LEVI,¹ M. MANERA,^{28,12} P. MARTINI,^{22,29,24} A. MEISNER,⁹ R. MIQUEL,^{11,12} J. MOUSTAKAS,³⁰ A. MUÑOZ-GUTIÉRREZ,⁸ S. NADATHUR,⁷ N. PALANQUE-DELABROUILLE,^{21,1} W. J. PERCIVAL,^{31,32,33} MATTHEW M. PIERI,³⁴ C. POPPETT,^{1,35,10} F. PRADA,³⁶ I. PÉREZ-RÀFOLS,³⁷ G. ROSSI,³⁸ E. SANCHEZ,³⁹ D. SCHLEGEL,¹ H. SEO,⁴⁰ J. SILBER,¹ D. SPRAYBERRY,⁹ G. TARLÉ,⁴¹ AND B. A. WEAVER⁹

¹Lawrence Berkeley National Laboratory, 1 Cyclotron Road, Berkeley, CA 94720, USA

²NASA Einstein Fellow

³Department of Physics, Boston University, 590 Commonwealth Avenue, Boston, MA 02215 USA

⁴Dipartimento di Fisica “Aldo Pontremoli”, Università degli Studi di Milano, Via Celoria 16, I-20133 Milano, Italy

⁵INAF-Osservatorio Astronomico di Brera, Via Brera 28, 20122 Milano, Italy

⁶Department of Physics & Astronomy, University College London, Gower Street, London, WC1E 6BT, UK

⁷Institute of Cosmology and Gravitation, University of Portsmouth, Dennis Sciama Building, Portsmouth, PO1 3FX, UK

⁸Instituto de Física, Universidad Nacional Autónoma de México, Circuito de la Investigación Científica, Ciudad Universitaria, Cd. de México C. P. 04510, México

⁹NSF NOIRLab, 950 N. Cherry Ave., Tucson, AZ 85719, USA

¹⁰University of California, Berkeley, 110 Sproul Hall #5800 Berkeley, CA 94720, USA

¹¹Institució Catalana de Recerca i Estudis Avançats, Passeig de Lluís Companys, 23, 08010 Barcelona, Spain

¹²Institut de Física d’Altes Energies (IFAE), The Barcelona Institute of Science and Technology, Edifici Cn, Campus UAB, 08193, Bellaterra (Barcelona), Spain

¹³Departamento de Física, Universidad de los Andes, Cra. 1 No. 18A-10, Edificio Ip, CP 111711, Bogotá, Colombia

¹⁴Observatorio Astronómico, Universidad de los Andes, Cra. 1 No. 18A-10, Edificio H, CP 111711 Bogotá, Colombia

¹⁵Institut d’Estudis Espacials de Catalunya (IEEC), c/ Esteve Terradas 1, Edifici RDIT, Campus PMT-UPC, 08860 Castelldefels, Spain

¹⁶Institute of Space Sciences, ICE-CSIC, Campus UAB, Carrer de Can Magrans s/n, 08913 Bellaterra, Barcelona, Spain

¹⁷University of Virginia, Department of Astronomy, Charlottesville, VA 22904, USA

¹⁸Fermi National Accelerator Laboratory, PO Box 500, Batavia, IL 60510, USA

¹⁹Department of Astronomy, The University of Texas at Austin, 2515 Speedway Boulevard, Austin, TX 78712, USA

²⁰Institut d’Astrophysique de Paris, 98 bis boulevard Arago, 75014 Paris, France

²¹IRFU, CEA, Université Paris-Saclay, F-91191 Gif-sur-Yvette, France

²²Center for Cosmology and AstroParticle Physics, The Ohio State University, 191 West Woodruff Avenue, Columbus, OH 43210, USA

²³Department of Physics, The Ohio State University, 191 West Woodruff Avenue, Columbus, OH 43210, USA

²⁴The Ohio State University, Columbus, 43210 OH, USA

²⁵Department of Physics, The University of Texas at Dallas, 800 W. Campbell Rd., Richardson, TX 75080, USA

²⁶Department of Physics and Astronomy, University of California, Irvine, 92697, USA

²⁷Sorbonne Université, CNRS/IN2P3, Laboratoire de Physique Nucléaire et de Hautes Energies (LPNHE), FR-75005 Paris, France

²⁸Departament de Física, Serra Húnter, Universitat Autònoma de Barcelona, 08193 Bellaterra (Barcelona), Spain

²⁹Department of Astronomy, The Ohio State University, 4055 McPherson Laboratory, 140 W 18th Avenue, Columbus, OH 43210, USA

³⁰Department of Physics and Astronomy, Siena University, 515 Loudon Road, Loudonville, NY 12211, USA

³¹Department of Physics and Astronomy, University of Waterloo, 200 University Ave W, Waterloo, ON N2L 3G1, Canada

³²Perimeter Institute for Theoretical Physics, 31 Caroline St. North, Waterloo, ON N2L 2Y5, Canada

³³Waterloo Centre for Astrophysics, University of Waterloo, 200 University Ave W, Waterloo, ON N2L 3G1, Canada

³⁴Aix Marseille Univ, CNRS, CNES, LAM, Marseille, France

³⁵Space Sciences Laboratory, University of California, Berkeley, 7 Gauss Way, Berkeley, CA 94720, USA

³⁶Instituto de Astrofísica de Andalucía (CSIC), Glorieta de la Astronomía, s/n, E-18008 Granada, Spain

³⁷Departament de Física, EEBE, Universitat Politècnica de Catalunya, c/Eduard Maristany 10, 08930 Barcelona, Spain

³⁸Department of Physics and Astronomy, Sejong University, 209 Neungdong-ro, Gwangjin-gu, Seoul 05006, Republic of Korea

³⁹CIEMAT, Avenida Complutense 40, E-28040 Madrid, Spain

⁴⁰Department of Physics & Astronomy, Ohio University, 139 University Terrace, Athens, OH 45701, USA

⁴¹University of Michigan, 500 S. State Street, Ann Arbor, MI 48109, USA

ABSTRACT

We present a measurement of Baryon Acoustic Oscillations (BAO) in the cross-correlation of triply ionized carbon (C IV) absorption with the positions of quasars (QSO) and Emission Line Galaxies (ELG). We use quasars and ELGs from the second data release (DR2) of the Dark Energy Spectroscopic Instrument (DESI) survey. Our data sample consists of 2.5 million quasars, 3.1 million ELGs, and the C IV absorption is measured along the line of sight of 1.5 million high redshift quasars with $z > 1.3$. We measure the isotropic BAO signal at 4.2σ for the CIV×QSO cross-correlation. This translates into a 3.0% precision measurement of the ratio of the isotropic distance scale, D_V , and the sound horizon at the drag epoch, r_d , with $D_V/r_d(z_{\text{eff}} = 1.92) = 30.3 \pm 0.9$. We make the first detection of the BAO feature in the CIV×ELG cross-correlation at a significance of 2.5σ and find $D_V/r_d(z_{\text{eff}} = 1.47) = 24.6 \pm 1.0$.

1. INTRODUCTION

Baryon Acoustic Oscillations (BAO) have been used to study the expansion history of the Universe for two decades (Weinberg et al. 2013; Eisenstein et al. 2007). These oscillations are sound waves that formed due to perturbations in the primordial plasma in the early universe. The sound waves were “frozen” into the matter distribution during recombination and can be seen in the distribution of matter at large scales in the universe (Weinberg et al. 2013; Hu & Sugiyama 1996; Eisenstein & Hu 1998; Eisenstein et al. 2007; Eisenstein & Bennett 2008). The BAO scale, once normalized to the sound horizon r_d , is a standard cosmological ruler and serves as a tool for probing the expansion of the universe.

Typical BAO measurements use galaxies as tracers of the matter distribution through the two-point correlation function. This correlation function quantifies the probability of two tracers being separated by a given distance, generally measured in comoving coordinates for a choice of fiducial cosmology. Using various tracers at different redshifts for measurements of BAO probe the Universe at different energy densities, allowing for comparisons between a more matter dominated Universe versus a dark energy dominated Universe.

The precision of BAO measurements with galaxies at high redshifts is restricted by the low number density of sources that are bright enough to secure their redshifts, and by the absence of bright emission lines redshifted to wavelengths shorter than 1 micron for instruments equipped with silicon Charge-Coupled Device (CCD) detectors. To mitigate this, spectroscopic surveys have incorporated other tracers, such as high redshift quasars (with $z \geq 2$) and the Lyman- α forest, that allow for precise BAO measurements at redshifts that were unattainable with galaxy surveys alone.

The most recent set of BAO measurements comes from the Dark Energy Spectroscopic Instrument (DESI; DESI Collaboration et al. 2016, 2022). With the Data Release 1 (DR1; DESI Collaboration et al. 2025a), DESI released BAO measurements with galaxies and quasars (Adame et al. 2025a) and the Lyman- α forest (Adame et al. 2025b), and cosmological constraints from full-shape measurements (Adame et al. 2025c) and from BAO (Adame et al. 2025d). Most recently, DESI released updated analyses using Data Release 2 (DR2) for measurements of BAO with the Lyman- α forest (DESI Collaboration et al. 2025b, hereafter DESI-2025-I) and cosmological constraints with galaxies and quasars (DESI Collaboration et al. 2025c, hereafter DESI-2025-II). These updated results confirm what was found in the DESI Year 1 results that dark energy may be evolving.

Galaxies, such as Emission Line Galaxies (ELG) and Luminous Red Galaxies (LRG), and the Lyman- α forest are not the only tracers that can be used to measure BAO. In fact, as efforts to observe the universe at high redshift have increased, BAO measurements with other tracers, like Lyman-break galaxies (LBG) and Lyman-alpha emitting galaxies (LAE), have become increasingly common as instruments become more powerful, allowing for the precision and density needed for fainter tracers (Herrera-Alcantar et al. 2025; White et al. 2024; Sailer et al. 2021; Ferraro et al. 2022; Ouchi et al. 2020).

One tracer that has been infrequently explored is the doublet transition of triply ionized carbon (C IV). Often classified as a metal or a contaminant in Lyman- α forest analyses, C IV offers a unique window for measurements at different redshifts than those with galaxies, quasars, and the Lyman- α forest. C IV has a strong doublet ($\lambda_{\text{RF}} = 1548.20, 1550.78 \text{ \AA}$) and is the dominant absorber between the Lyman- α and C IV emission lines (Pieri 2014). In optical spectra, the Lyman- α forest can only be seen

at redshifts $z > 2$, however, DESI can observe the C IV doublet down to $z \sim 1.3$. This allows for measurements at various effective redshifts when correlated with different tracer positions.

When cross-correlated with quasars, a BAO measurement with the C IV forest allows for additional constraints on cosmological parameters at an effective redshift of $z_{\text{eff}} \sim 2$, directly in the redshift gap between the measurement from the QSO auto-correlation and the Lyman- α forest (see Figure 6 of [DESI-2025-II](#)). Cross-correlating the C IV forest with the DESI Emission Line Galaxy (ELG) sample would allow for an additional measurement around $z_{\text{eff}} \sim 1.5$. The DESI ELG sample probes the Universe over the $0.6 < z < 1.6$ range and brings the tightest cosmological constraints from DESI ([Raichoor et al. 2023](#)).

This work is largely based on [Blomqvist et al. \(2018\)](#), who presented the first BAO measurement using the cross-correlation of the C IV forest with quasars from the Sloan Digital Sky Survey (SDSS) data release 14 (DR14) ([Abolfathi et al. 2018](#)). [Gontcho A Gontcho et al. \(2018\)](#) performed a similar study, using the SDSS-DR12 dataset ([Alam et al. 2015](#)) where they measured the effective optical depth $\bar{\tau}_c(z)$ and the linear bias parameters β_c and b_{Fc} of the C IV forest. The nature of the C IV doublet (as well as other metal doublets) allows for automated searches in quasar spectra to create catalogs that can be used in large-scale studies of metals in the universe ([Anand et al. 2025; Napolitano et al. 2023; Anand et al. 2021](#)). Using such a technique, [Anand et al. \(2025\)](#) and [Cooksey et al. \(2013\)](#) found that the abundance of Carbon in the universe is larger at late times than at earlier times.

In this work, we present a BAO measurement from cross-correlations with the C IV forest using the 3-year main survey dataset from DESI DR2, collected between May 14th, 2021 and April 9th, 2024, using both quasars and ELGs as tracers. We begin in section 2 with a brief description of the datasets used in the analysis, including how we extract the C IV forest fluctuations from the quasar spectra. In section 3, we present a summary of how we measure the correlations. Our method follows what was done in [Blomqvist et al. \(2018\)](#) with updated analysis components following [DESI-2025-I](#). We also present the measured correlation functions from quasars and ELGs and discuss contamination from metals. In section 4 we present our main result and discuss the choices made for our baseline analysis. We also discuss validation tests on correlations with both the quasar and ELG samples. We conclude and suggest future studies in section 5.

2. DATA SAMPLE

DESI is a ground-based Stage-IV dark energy experiment that began its main survey in 2021. Over the course of the 8-year survey, DESI will construct the largest 3D map of the Universe by collecting redshifts for over 60 million extragalactic sources. This map will allow for studies of the large-scale structure in the Universe and the effects of dark energy on the expansion of the universe.

DESI is a multi-object fiber-fed spectroscopic instrument located at the Mayall Telescope at Kitt Peak National Observatory (KPNO) in the Tohono O'odham Nation in Arizona. Light from distant objects reflects off the 4-meter mirror into the optical corrector system and lands on the focal plane. The focal plane consists of 5,000 robotically controlled fiber positioners that simultaneously point at targets on the sky. Optical fibers route the light collected from the positioners to the spectrographs. There are 10 spectrographs, each with 3 channels (blue, red, and near-infrared), spanning wavelengths from 3600 Å to 9800 Å. The spectra are then processed by the spectroscopic pipeline ([Guy et al. 2023](#)). More information about the DESI instrument and the spectrographs, the optical corrector, the focal plane, and the fiber system can be found in [DESI Collaboration et al. \(2022\)](#), [Miller et al. \(2024\)](#), [Silber et al. \(2023\)](#), and [Poppett et al. \(2024\)](#), respectively.

Over the course of the 8-year main survey, DESI will cover more than 14,000 square degrees of the sky. There are two programs that make up the main survey: dark and bright. The dark program targets galaxies (emission line galaxies and luminous red galaxies) and quasars when conditions are good, while the bright program targets bright galaxies and Milky Way stars when conditions are not good enough for the dark program ([Schlafly et al. 2023](#)).

In this paper, we use the DR2 dataset composed of data from the first three years of the DESI main survey. There are approximately twice as many quasars and nearly three times as many ELGs as there were in DR1.

2.1. Quasar Sample

We use a modified version of the DESI DR2 quasar catalog used in [DESI-2025-I](#). The catalog is constructed based on results from the spectroscopic pipeline and the redshift fitting software `Redrock` ([Bailey 2025](#)). All targets are classified as either a galaxy, quasar, or star by `Redrock` and their redshift is measured. Quasar targets and objects classified as a quasar by `Redrock` are run through two additional afterburners. The first is the Mg II afterburner ([Chaussidon et al. 2023](#)) that searches

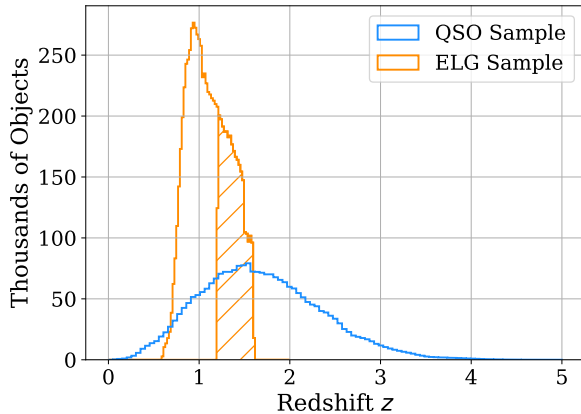


Figure 1. Redshift distributions of the quasar (blue) and the ELG catalogs (orange) used in this work. Only the ELGs with $z > 1.2$ will contribute to the cross-correlation and those redshifts are highlighted by the hatched histogram.

for broad Mg II emission in quasar targets that Redrock identified as a galaxy. The second is QuasarNet (Green et al. 2025; Busca & Balland 2021), which uses a convolutional neural network to automatically classify quasar spectra.

The DR2 quasar catalog consists of 2,776,520 quasars. We modify this catalog and remove any quasars that are identified as Broad Absorption Line (BAL) quasars. BAL quasars have blueshifted absorption that is often coupled to C IV emission and these absorption troughs consequently affect the continuum in the C IV region. Though Ennesser et al. (2022) and Martini et al. (2025) showed that masking BAL features does not affect BAO measurements with the Lyman- α forest, quasars that have a BAL at the C IV emission line can have significant changes to the line profile that can lead to redshift errors. We identify BAL quasars with the BALFinder (Filbert et al. 2024; Martini et al. 2025; Guo & Martini 2019) and use the absorptivity index (AI) to select which BALs to exclude. We consider a quasar to be a BAL if it has $AI > 0$ and we exclude all BALs from our catalog. Our final quasar catalog consists of 2,498,218 quasars and the redshift distribution is shown in Figure 1 as the blue histogram.

2.2. Forest Samples

We define the C IV region as the spectral region between $1420 \text{ \AA} \leq \lambda_{\text{RF}} < 1520 \text{ \AA}$ in rest frame wavelengths and we define the forest as the flux fluctuations due to C IV absorption in this region. This region avoids wavelengths close to the C IV and Si IV emission lines in the quasar spectra. Since quasar emission lines are broad, the wings of these lines can enter the forest region, es-

pecially C IV as it has a variable profile (e.g. Shen et al. 2016). We also apply a cut for forests that fall outside of the observed wavelength range $3600 \text{ \AA} \leq \lambda_{\text{OBS}} < 7600 \text{ \AA}$. The lower limit is set by the DESI spectrographs and the upper limit corresponds to the middle of the transition region between the red and near-infrared channels. This effectively provides a quasar redshift cut of $1.36 \leq z_q \leq 4.35$.

We also measure C IV flux fluctuations in the Si IV region, which we define as the spectral region between $1260 \text{ \AA} \leq \lambda_{\text{RF}} < 1375 \text{ \AA}$. The lower bound avoids the red wing of the Lyman- α and NV emission lines and the upper bound avoids the wing from the Si IV emission line. This corresponds to a quasar redshift cut of $1.6 \leq z \leq 5$. Figure 2 shows an example quasar spectrum from DR2 at $z = 3.26$. The C IV and Si IV regions are highlighted, as well as the Lyman- α and Lyman- β regions used in DESI-2025-I.

We use the average wavelength of the C IV doublet, $\lambda_c = 1549.06 \text{ \AA}$, to convert from spectral pixels to redshifts in each of the C IV and Si IV regions. We require each spectrum to have a number of valid pixels in the forest region with an integrated length larger than 25% of the total length of the forest region. For the C IV region, this corresponds to 90 pixels and 110 pixels for the Si IV region. The pixel size is 0.8 \AA (in the observer frame).

We mask areas of the spectra that are prone to contamination from sky lines and absorption lines for Calcium and Sodium present in the interstellar medium. Because we removed BAL quasars from the catalog, we do not need to mask BAL regions in either forest region. Martini et al. (2025) describes the updated strategy for masking BAL regions in the DR2 Lyman- α forest analysis. We discuss in section 4.3 the impact that this strategy has on our results when we include the BAL quasars. Unlike the DR2 Lyman- α analysis, we do not have to account for Damped Lyman- α Absorption (DLA) systems in this work. DLAs occur blueward of the Lyman- α emission line and will therefore not appear in the C IV and Si IV regions.

In order to measure flux fluctuations in the C IV region, we measure the flux transmission field δ_q for each quasar q as a function of observed wavelength:

$$\delta_q(\lambda) = \frac{f_q(\lambda)}{\bar{F}(\lambda)C_q(\lambda)} - 1, \quad (1)$$

where $f_q(\lambda)$ is the observed flux, $C_q(\lambda)$ is the unabsorbed quasar continuum, and $\bar{F}(\lambda)$ is the mean transmission. The method for estimating the unabsorbed continuum is described in detail in Ramírez-Pérez et al. (2024) and is performed with the `picca` software (du

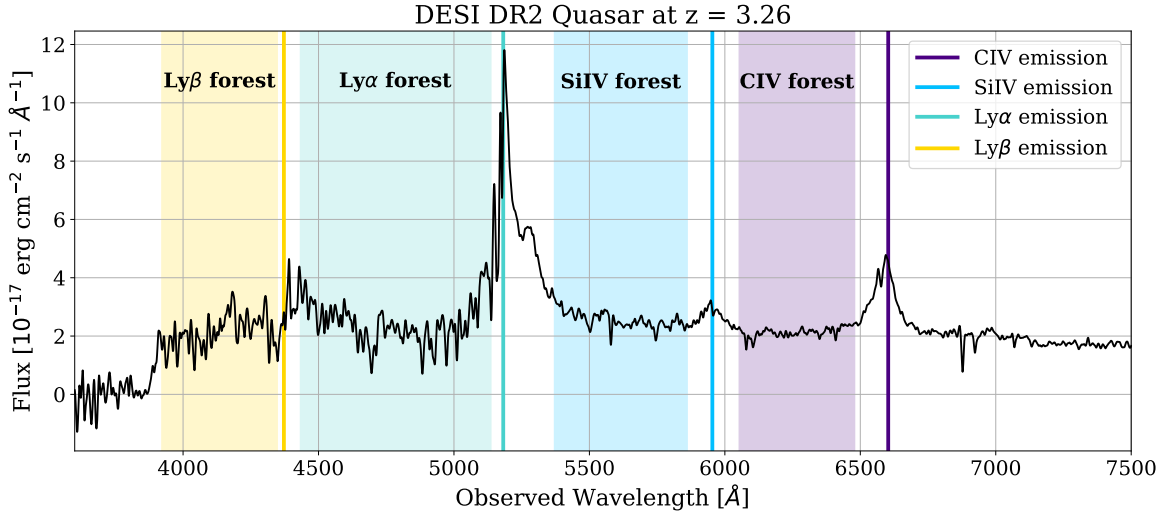


Figure 2. A smoothed quasar spectrum from the DESI DR2 dataset at $z = 3.26$ (TargetID = 39627334130598165). The spectrum shows the emission peaks and forest regions for the two areas typically used in BAO analyses: Ly α (green) and Ly β (yellow). In this analysis, we measure CIV absorption in the CIV region (purple) from 1420 to 1520 Å in the quasar rest-frame, and in the SiIV region (blue) from 1260 to 1375 Å.

Mas des Bourboux et al. 2021). In short, the continuum fitting process consists of obtaining the mean expected flux, $\bar{F}(\lambda)C_q(\lambda)$, over several iterations. To simplify the process, the mean expected flux is assumed to be a universal function of rest-frame wavelength with a first-degree polynomial correction in $\log \lambda$:

$$\bar{F}(\lambda)C_q(\lambda) = \bar{C}(\lambda_{\text{RF}}) \left(a_q + b_q \frac{\Lambda - \Lambda_{\min}}{\Lambda_{\max} - \Lambda_{\min}} \right), \quad (2)$$

where $\Lambda \equiv \log \lambda$. This correction accounts for differences in quasar luminosity and spectral diversity as well as the redshift evolution of \bar{F} . This iterative process solves for $\bar{C}(\lambda_{\text{RF}})$, a_q , and b_q and also takes into account the pipeline noise and applies a correction to account for the intrinsic variance of each forest region. There is an additional parameter, η_{LSS} , that optimizes the weights assigned to each forest. For the Lyman- α forest, Ramírez-Pérez et al. (2024) found that the optimal value for $\eta_{\text{LSS}} = 7.5$. However, this value will change with different datasets, as it will depend on other properties that go into the weights calculation like the pipeline noise and the intrinsic variance in the particular forest region. Following the method in Ramírez-Pérez et al. (2024), we perform our own analysis of η_{LSS} for each of the CIV and SiIV regions and find $\eta_{\text{LSS}} = 20$ and $\eta_{\text{LSS}} = 12$ for the two forest regions, respectively.

After the above cuts are made and the continuum fitting process is complete, our CIV region sample contains 1,524,506 forests and the SiIV region sample has 1,130,354 forests.

2.3. Emission Line Galaxy Sample

Our sample of ELGs comes from the DESI DR2 large-scale structure (LSS) catalogs used in DESI-2025-II. The LSS catalog pipeline is detailed in Ross et al. (2025) (section 7.1). The ELG sample is split into two redshift bins spanning $0.8 < z < 1.1$ and $1.1 < z < 1.6$, containing 2.7 million and 3.8 million ELGs, respectively (DESI-2025-II). In this work, we use the clustering catalog for the full ELG sample. The clustering catalogs are the same as the full LSS catalogs; however, they remove extra columns and apply a cut to select only good spectroscopic observations. A good observation is one that has no Redrock ZWARN bits set (DESI Collaboration et al. 2024).

The ELG catalog consists of redshifts between $0.6 < z < 1.6$, though any object with a redshift less than $z \sim 1.2$ will not be included in the correlations as the comoving separation will be larger than the range we study. The distribution of redshifts is shown in Figure 1 as the orange histogram. The hatched histogram shows the objects with $z > 1.2$. We do not apply any other cuts to the catalog, and our final ELG sample contains 3.1 million objects.

3. ANALYSIS

We measure the cross-correlation function with CIV absorption in two regions: the CIV region and the SiIV region, which we refer to as side-band 2 (SB2) and side-band 1 (SB1), respectively, throughout the rest of this paper. We measure the cross-correlation in each side-band using both quasars and ELGs as tracers. We fol-

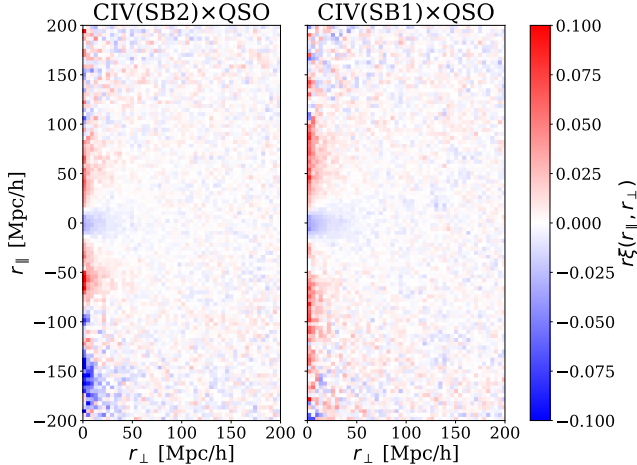


Figure 3. Two-dimensional correlation function shown as r_{\parallel} and r_{\perp} for the two correlations: CIV(SB2) \times QSO and CIV(SB1) \times QSO. The BAO feature is not easily seen by eye but is observed as a half ring at $r \sim 100 h^{-1}$ Mpc. Both correlations are multiplied by r for visualization purposes. There are oscillatory features at $r_{\parallel} < 0$ in CIV(SB2) caused by quasar redshift errors (discussed in section 4.2).

low the methods used in previous analyses to measure the correlation functions, calculate the distortion and covariance matrices, and model the contamination due to metals. The correlation and covariance calculations are the same as in Adame et al. (2025b), but improvements have since been made to the computation of the distortion and metal matrices. These improvements are described in Section 3 of DESI-2025-I. We calculate the correlations and the distortion matrix with `picca`¹. We follow the same method as DESI-2025-I to calculate the covariance. The metal matrices are calculated with `Vega` (Cuceu et al. 2023; du Mas des Bourboux et al. 2020) during the fit.

3.1. Correlations

We calculate the correlation function by binning in comoving coordinates along (r_{\parallel}) and across (r_{\perp}) the line of sight, extending out to $200 h^{-1}$ Mpc in both positive and negative r_{\parallel} and positive r_{\perp} . Because the cross-correlation is not symmetric and we need to extend to negative separations in r_{\parallel} , we define a positive separation along the line of sight when the quasar or ELG is in front of the C IV forest pixel. To calculate separations in comoving coordinates, we assume the Λ CDM cosmology from Planck Collaboration et al. (2020), hereafter “Planck2018”, as our fiducial cosmology. This is the same fiducial cosmology used in DESI-2025-I.

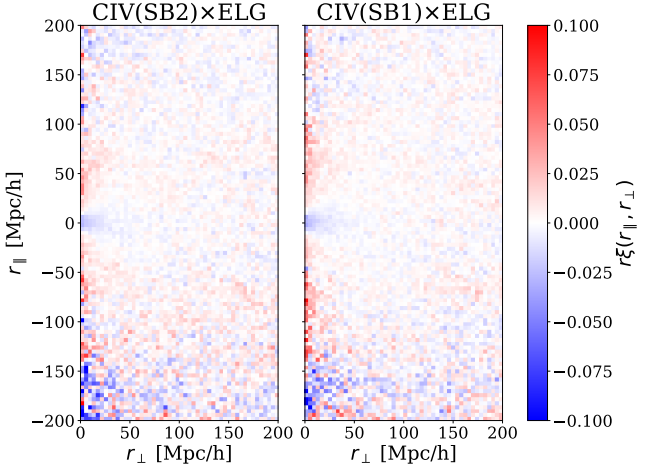


Figure 4. Two-dimensional correlation function shown as r_{\parallel} and r_{\perp} for the two correlations: CIV(SB2) \times ELG and CIV(SB1) \times ELG. The BAO feature is not easily seen by eye but is observed as a half ring at $r \sim 100 h^{-1}$ Mpc. Both correlations are multiplied by r for visualization purposes. The data is noisy so it is difficult to see any oscillatory features at $r_{\parallel} < 0$ in CIV(SB2).

We show the measured two-dimensional correlations in r_{\parallel} and r_{\perp} with quasars and ELGs for each side-band in Figures 3 and 4. We multiply the correlation by the total separation r and center the colorbar around zero for visualization purposes. The BAO can usually be seen as a half ring at $r \sim 100 h^{-1}$ Mpc, though the data here is noisy and it is harder to see. In SB2 in Figure 3, there are oscillatory features at small r_{\perp} for negative r_{\parallel} that are not present in SB1. We believe these oscillations are due to quasar redshift errors (Gordon et al. 2025; Youles et al. 2022) and we discuss how to mitigate them in section 4.2. These errors are also present in the ELG correlation in Figure 4, but the data is noisier and it is not as easily seen in the figure.

Figure 5 shows the two-dimensional correlation of Figures 3 and 4 reduced to a weighted one-dimensional correlation that is averaged over bins of total separation $r = (r_{\parallel}^2 + r_{\perp}^2)^{1/2}$. The wedges are defined by a range of the cosine between r and the line of sight, $\mu = r_{\parallel}/r$. $|\mu| = 1$ is along the line of sight while $\mu = 0$ is across the line of sight. In this case, we are compressing the data and best fit model (black line) from both SB2 and SB1 into one wedge between $-0.95 \leq \mu \leq 1.0$ for quasars (blue points) and ELGs (orange points). These wedges are not used for fitting the data. The BAO feature can be seen as a trough near $100 h^{-1}$ Mpc.

3.2. Contamination from Other Transition Lines

There are small contributions from other absorption by metals in the intergalactic medium (IGM) that can

¹ `picca`: <https://github.com/igmhub/picca/tree/v9.13.0>

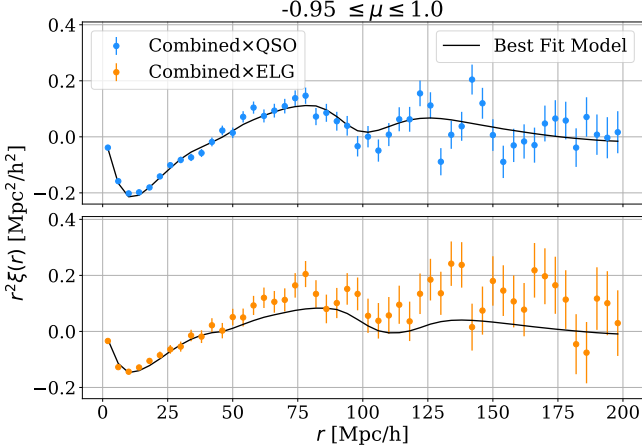


Figure 5. Weighted one-dimensional correlation averaged over bins of total separation r and lines of sight μ when using quasars (blue) and ELGs (orange) as tracers. For each tracer, we are showing the correlation when combining the two side-bands, and we compress the two-dimensional data and best-fit model into one wedge between $-0.95 \leq \mu \leq 1.0$. We multiply both correlations by r^2 for visualization purposes. The BAO “peak” is seen as a trough near $100 h^{-1}$ Mpc for both tracers.

produce additional signal in the cross-correlations. Historically, “metals” refers to any element that is not neutral hydrogen, meaning that CIV itself would be classified as a metal. In this work, we define metal absorption as absorption caused by transitions other than CIV.

Metal contamination in the Lyman- α forest has been extensively studied (Guy et al. 2025; Yang et al. 2022; Bautista et al. 2017; Pieri et al. 2014), however, it has been studied less so in the CIV and SiIV regions. Following Blomqvist et al. (2018), we identify metal contamination in the CIV and SiIV regions by measuring the one-dimensional auto-correlation function, ξ_{1D} , using the forest samples described in section 2.2. Figure 6 shows ξ_{1D} as a function of wavelength ratio λ_1/λ_2 for the CIV region (SB2, indigo) and the SiIV region (SB1, blue).

There are prominent peaks from correlations between the CIV and SiIV doublets, CIV- and SiIV-metal, and metal-metal pairs. Since we are measuring correlations using CIV as the absorber, only the peaks associated with either line of the CIV doublet will produce contributions to the measured correlations. These lines are SiII(1527) ($\lambda = 1526.71$ Å) and FeII(1608) ($\lambda = 1608.45$ Å) and are highlighted with purple dashed lines in Figure 6.

The contributions from the two metal lines will appear in both the QSO and ELG cross-correlations, as they are dependent on the absorber (CIV) and not the tracer. The maximum contributions from the different metals

occur at different redshifts along the line of sight at $r_\perp = 0$ and $r_\parallel \approx \frac{c}{H(z)}(1+z)(\lambda_m - \lambda_{\text{CIV}})/\lambda_{\text{CIV}}$. The r_\parallel values for the CIV-metal transition are given in Table 1.

4. RESULTS

The model used to measure the BAO scale has been well described and widely studied in previous works (du Mas des Bourboux et al. (2020); Gordon et al. (2023); Bault et al. (2025); Adame et al. (2025b); DESI Collaboration et al. (2025b); etc.). We follow the same prescription here and discuss key differences in this work in section 4.1. We use the Vega² package to model the correlations and metals and for parameter inference.

The BAO parameters are defined as:

$$\alpha_\parallel = \frac{[D_H(z_{\text{eff}})/r_d]}{[D_H(z_{\text{eff}})/r_d]_{\text{fid}}} \quad \text{and} \quad \alpha_\perp = \frac{[D_M(z_{\text{eff}})/r_d]}{[D_M(z_{\text{eff}})/r_d]_{\text{fid}}}, \quad (3)$$

where z_{eff} is the effective redshift of the measurement and “fid” represents the Planck2018 fiducial cosmology used in this work where $\alpha_\parallel = \alpha_\perp = 1$. $D_H(z)$ is the Hubble distance and is defined as

$$D_H(z) = \frac{c}{H(z)}, \quad (4)$$

and $D_M(z)$ is the transverse comoving distance. For a flat universe, D_M is defined as

$$D_M(z) = \frac{c}{H_0} \int_0^z \frac{dz'}{H(z')/H_0}. \quad (5)$$

When there is not enough signal to measure BAO from α_\parallel and α_\perp , we can instead measure BAO from the isotropic signal:

$$\alpha_{\text{iso}} = \frac{[D_V(z_{\text{eff}})/r_d]}{[D_V(z_{\text{eff}})/r_d]_{\text{fid}}}, \quad (6)$$

where $D_V(z)$ is the spherically-averaged distance over the radial and transverse directions and is defined as:

$$D_V(z) \equiv [z D_M(z)^2 D_H(z)]^{1/3} \quad (7)$$

In equations 3 and 6, r_d is the sound horizon at the drag epoch. The distances D_H , D_M , and D_V are inferred relative to r_d , the constrained quantities are the ratios D_H/r_d , D_M/r_d , or D_V/r_d . In all results discussed in this paper, we are measuring isotropic BAO unless otherwise specified.

4.1. Baseline Fit

We present results for BAO measurements with two separate tracers: one with quasars and one with ELGs.

² Vega: <https://github.com/andreicuceu/vega> version 1.3.1

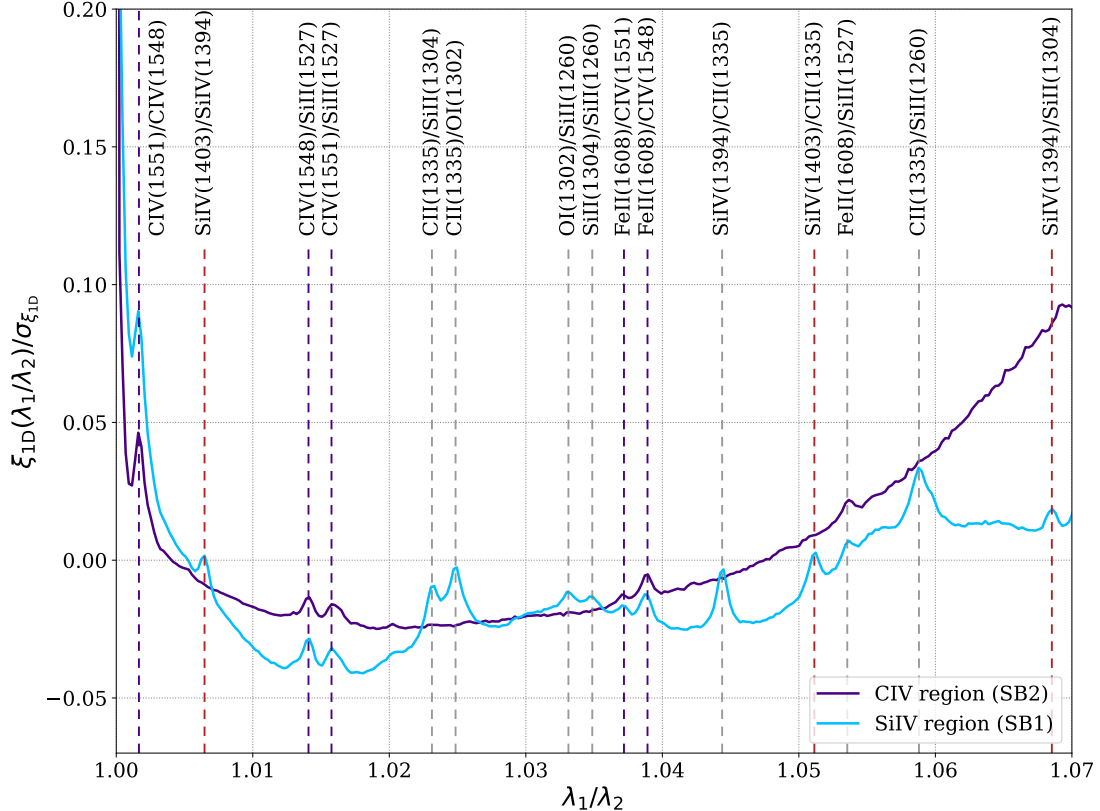


Figure 6. One-dimensional auto-correlation function ξ_{1D} as a function of wavelength ratio λ_1/λ_2 for pixel pairs in SB2 (indigo) and SB1 (blue), ordered such that $\lambda_1 > \lambda_2$. Vertical dashed lines indicate prominent correlations involving the CIV doublet (indigo), the SiIV doublet (red), and other metal-metal transitions (grey). The metals involving the CIV doublet are the only lines that we include in our correlations. These are FeII(1608) and SiII(1527).

Absorber pair	$\lambda_1 [\text{\AA}]$	$\lambda_2 [\text{\AA}]$	λ_1/λ_2	$r_{\parallel} [\text{h}^{-1} \text{Mpc}]$
CIV(1548)-Si II(1527)	1548.20	1526.71	1.014	-41.22
CIV(1551)-Si II(1527)	1550.78	1526.71	1.016	-46.08
Fe II(1608)-CIV(1548)	1608.45	1548.20	1.039	115.53
Fe II(1608)-CIV(1551)	1608.45	1550.78	1.037	110.41

Table 1. Metal correlations involving the CIV doublet lines for the two metal species identified in Figure 6 that will impact the CIV(SB2) and CIV(SB1) correlations. The second and third columns list the rest-frame wavelength of the absorber-metal pair. The fourth column gives the wavelength ratio of the two lines. The final column gives the line-of-sight separation calculated at $z = 2$ for the quasar measurement. These metal correlations will occur at slightly different separations (using $z = 1.5$) for the ELG measurements.

The two quasar cross-correlations in the baseline fit include CIV absorption in SB2 (CIV(SB2)×QSO) and in SB1 (CIV(SB1)×QSO). Similarly for ELGs, our baseline fit contains the two cross-correlations with CIV absorption in SB2 (CIV(SB2)×ELG) and in SB1 (CIV(SB1)×ELG). We also include the covariance matrix to account for small cross-covariance between the two correlation functions for each tracer. Following DESI-2025-I, we fit all correlations over the range $30 < r < 180 \text{ h}^{-1} \text{ Mpc}$. For both the quasar and ELG measurements, we exclude the wedge region along the line of

sight at negative r_{\parallel} (between $-1.0 \leq \mu < -0.95$) in the SB2 region only. We discuss why later in this section.

Our baseline fit contains 7 free parameters: the BAO parameter α_{iso} (8 free parameters when fitting for α_{\parallel} and α_{\perp}), the bias and redshift space distortion (RSD) parameters for the CIV forest: $b_{\text{CIV}(\text{eff})}$ and $\beta_{\text{CIV}(\text{eff})}$, the bias parameters for the two metal species identified in section 3.2: $b_{\text{FeII}(1608)}$ and $b_{\text{SiII}(1527)}$, and two parameters that describe redshift errors: σ_v and Δr_{\parallel} , which account for peculiar velocities and systematic shifts in redshifts (Bault et al. 2025) for each tracer. We fix

$\beta_{\text{FeII}(1608)}$ and $\beta_{\text{SiII}(1527)}$ to 0.5, as done in many previous analyses (including Blomqvist et al. (2018), du Mas des Bourboux et al. (2020), Adame et al. (2025b), and DESI-2025-I) and based on the results from Font-Ribera & Miralda-Escudé (2012). The SiII(1527) metal line appears strongest in the correlations at $(r_{\perp}, r_{\parallel}) = (0, \sim 45) h^{-1} \text{ Mpc}$. This point is in the wedge region that is excluded from SB2 in the fit, and therefore $b_{\text{SiII}(1527)}$ is poorly constrained. We mitigate this by adding a Gaussian prior using the best-fit value from the CIV(SB1) fits for each tracer as the $-1.0 \leq \mu < -0.95$ wedge is not masked in this region. Because CIV is a doublet, there are additional contributions to the σ_v parameter that cause it to be poorly constrained. We therefore add a Gaussian prior to σ_v using the value from DESI-2025-I. Future work should look to improve on the σ_v prior for the ELG measurements. ELG redshifts in DESI are more precise as the redshift is determined by the [O II] doublet. Inherently, this means that the σ_v value for ELGs would be smaller than that of quasars. However, given the contribution from the CIV doublet to σ_v , we choose to use the same prior for both the quasar and ELG measurements.

We fix the quasar or ELG bias (b_q or b_e), as it is degenerate with the bias of the CIV forest, to the value calculated at the effective redshift for each tracer. The redshift evolution of the tracer bias is given by

$$b_t(z) = b_t(z_{\text{eff}}) \left(\frac{1+z}{1+z_{\text{eff}}} \right)^{\gamma-1}. \quad (8)$$

For quasars, $\gamma = 1.44$ (du Mas des Bourboux et al. 2019) and for the Lyman- α forest $\gamma = 2.9$ (McDonald et al. 2006). We estimate $\gamma_{\text{CIV}} = 1.5$ by measuring b_{CIV} at $z_{\text{eff}} = 1.92$ and $z_{\text{eff}} = 1.47$ and fitting for γ in equation 8. For ELGs, we used equation C.2 from Chaussidon et al. (2025) (with $a = 0.15$ and $b = 0.59$) and fit it with equation 8 between $1.0 < z < 2.5$ and found $\gamma_{\text{ELG}} = 1.3$.

We present a result of the BAO measurement using the isotropic signal. Our best fit value of α_{iso} from the combined fit with quasars is:

$$\alpha_{\text{iso}} = 1.031 \pm 0.030, \quad (9)$$

with a reduced χ^2 of $5808.76/(5891 - 7) = 0.987$ and a fit probability of 75.5%. We show the likelihood on α_{iso} for the combined fit, as well as the individual side band fits, in Figure 7. We quantify the detection of this BAO measurement by fitting a model with no BAO for the combined fit. We find a 4.2σ detection of the BAO signal from the measurement with quasars.

For ELGs, the best fit value for isotropic BAO from the combined fit is:

$$\alpha_{\text{iso}} = 0.953 \pm 0.038, \quad (10)$$

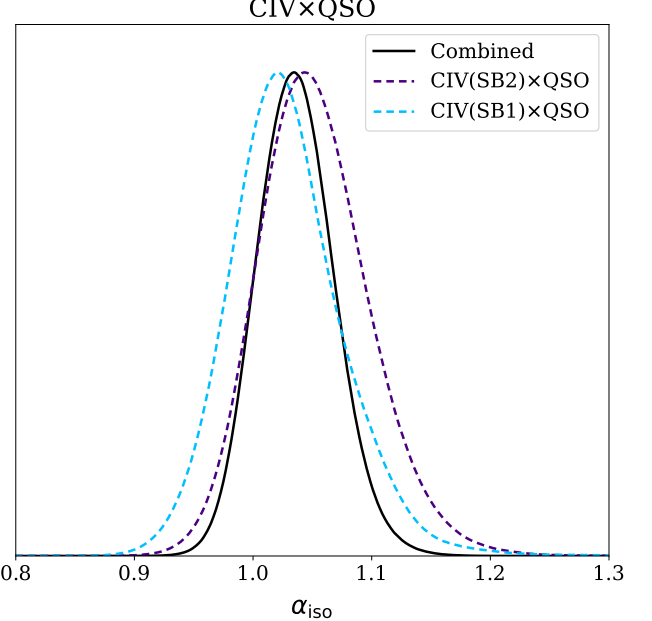


Figure 7. Likelihood of α_{iso} from the combined fit of the CIVxQSO cross-correlation (solid black line) as well as for fits to the individual CIV(SB2)xQSO (purple dashed line) and CIV(SB1)xQSO (blue dashed line) side bands.

with a reduced χ^2 of $6116.76/(5891 - 7) = 1.039$ and a fit probability of 1.7%. We show the likelihood of α_{iso} for the combined fit with ELGs and the two side bands in Figure 8. We measure BAO at 2.5σ significance from the measurement with ELGs.

Hadzhiyska et al. (2025) and de Belsunce et al. (2025) have investigated systematic uncertainties on the BAO shift from Lyman- α forest measurements when using linear theory. Following these results, DESI-2025-I added a systematic uncertainty of $\Delta\alpha_{\parallel} = 0.3\%$, $\Delta\alpha_{\perp} = 0.3\%$ to the covariance matrix. We expect the systematic uncertainty for non-linear clustering in this work to be similar to 0.3%; however, our errors are 10 times larger at 3% so we do not include a systematic uncertainty in our analysis. We also perform numerous validation tests, discussed in Section 4.3, that do not indicate any other source of significant systematic uncertainties.

The results for the best fit parameters for the combined fits and fits to CIV(SB2) and CIV(SB1) for the two tracers, as well as the priors used, are given in Table 2. All parameters have a flat prior except for σ_v , which has a Gaussian prior given by values from the combined fit from DESI-2025-I, and $b_{\text{SiII}(1527)}$, which has a Gaussian prior for the combined fit and the fit to SB2 given by the best-fit value from SB1. We show the agreement between parameters for the combined and two individual fits for the two tracers in Figures 12 and 13 in Appendix

Parameter	Priors	Best fit - QSO			Best fit - ELG		
		CIV(SB2)	CIV(SB1)	Combined	CIV(SB2)	CIV(SB1)	Combined
α_{iso}	$\mathcal{U}[0.5, 1.5]$	1.05 ± 0.05	1.02 ± 0.04	1.032 ± 0.030	0.92 ± 0.04	1.09 ± 0.06	0.95 ± 0.04
$b_{\text{CIV,eff}}$	$\mathcal{U}[-2.0, 0.0]$	-0.0115 ± 0.0008	-0.0133 ± 0.0006	-0.0129 ± 0.0005	-0.0131 ± 0.0014	-0.0124 ± 0.0008	-0.0123 ± 0.0007
$\beta_{\text{CIV,eff}}$	$\mathcal{U}[0.0, 4.0]$	0.59 ± 0.14	0.45 ± 0.09	0.46 ± 0.07	0.25 ± 0.18	0.20 ± 0.13	0.24 ± 0.11
$10^3 b_{\text{FeII}(1608)}$	$\mathcal{U}[-0.2, 0.0]$	-0.38 ± 0.20	-0.56 ± 0.20	-0.47 ± 0.14	-0.59 ± 0.20	-0.41 ± 0.18	-0.41 ± 0.14
$10^3 b_{\text{SIII}(1527)}$	$\mathcal{N}[-1.49, 0.18]$ $\mathcal{N}[-1.60, 0.27]$	-1.23 ± 0.17	-1.50 ± 0.18	-1.32 ± 0.12	-	-1.51 ± 0.27	-1.60 ± 0.28
$\sigma_v (h^{-1} \text{ Mpc})$	$\mathcal{N}[3.18, 0.5]$	3.2 ± 0.5	3.4 ± 0.5	3.3 ± 0.5	3.1 ± 0.5	3.1 ± 0.5	3.0 ± 0.5
$\Delta r_{\parallel} (h^{-1} \text{ Mpc})$	$\mathcal{U}[-5.0, 5.0]$	-0.9 ± 1.0	0.0 ± 0.7	0.1 ± 0.6	3.4 ± 1.1	-0.3 ± 0.6	0.5 ± 0.6
z_{eff}	-	1.97	1.87	1.92	1.47	1.47	1.47
χ^2_{min}	-	2684.60	3109.73	5808.76	2909.94	3193.43	6116.76
N_{bin}	-	2789	3102	5891	2789	3102	5891
N_{param}	-	7	7	7	7	7	7
probability	-	0.91	0.42	0.75	0.04	0.11	0.01

Table 2. Best-fit baseline results for CIV(SB2), CIV(SB1), and the combined fit for both the QSO and ELG tracers when fitting for isotropic BAO. The first column lists the parameters in the fit and the second column lists the priors used. Separate priors are used on $b_{\text{SIII}(1527)}$ when fitting with quasars or ELGs. The rest of the columns give the best-fit results for each parameter depending on which tracer is used. The first three columns give results for quasars while the last three columns give results for ELGs. The bottom section of the table gives the effective redshift, χ^2 , the number of data points in the fit, the number of free parameters, and the fit probability.

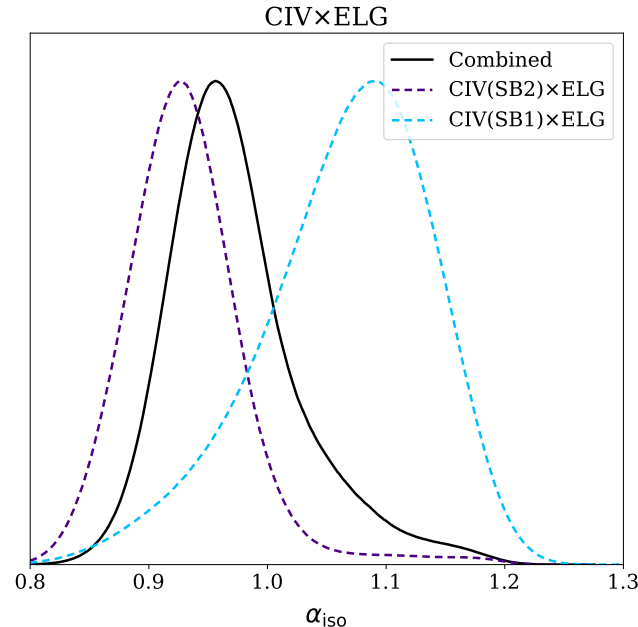


Figure 8. Likelihood of α_{iso} from the combined fit of the CIVxELG cross-correlation (solid black line) as well as for fits to the individual CIV(SB2)xELG (purple dashed line) and CIV(SB1)xELG (blue dashed line) side bands.

A. For both measurements, all parameters show a good agreement between the three fits.

Our results from the CIVxQSO measurement are in good agreement with the results from Blomqvist et al. (2018). They measured BAO to 6% precision at a significance of 1.7σ . We have improved the uncertainty of α_{iso} by a factor of 2 and have increased the significance of the detection by over 2σ . Our results for σ_v and Δr_{\parallel}

differ, however, this is not unexpected as the templates and method used to estimate quasar redshifts have improved (Bault et al. 2025; Brodzeller et al. 2023).

4.2. Goodness of Fit

We explore further the fit to the quasar measurement by studying the normalized residuals of the best fit model and the measured correlations, $(\xi_D - \xi_M)/\sigma_\xi$, for the two correlation functions where ξ_D is the measured correlation, ξ_M is the best fit model, and σ_ξ is the uncertainty of the correlation and is defined as the square root of the diagonal of the covariance matrix. The two-dimensional residuals for each correlation are shown in Figure 9. The area to the left of the black line is the wedge along the line of sight at negative r_{\parallel} (between $-1.0 \leq \mu < -0.95$) that is excluded from the fit.

For the quasar measurement, we find no significant disagreement between the data and the model in SB1. However, in SB2 we see oscillatory structure from $-180 < r_{\parallel} < -50 h^{-1} \text{ Mpc}$ along the line of sight ($r_{\perp} \sim 0 h^{-1} \text{ Mpc}$). These oscillations are the result of quasar redshift errors producing spurious correlations during the continuum fitting process. The r_{\parallel} where these correlations between quasar-pixel pairs in CIV(SB1) are strongest is larger than $200 h^{-1} \text{ Mpc}$ and, therefore, are not visible in the right panel of Figure 9. The oscillations are also present in the cross-correlation with ELGs, though the measurement is noisier and it is harder to see by eye.

Casas et al. (2025) showed a small bias on α_{\parallel} on the order of 0.5% produced by spurious correlations from quasar redshift errors during the continuum fitting process. Gordon et al. (2025) developed a method to re-

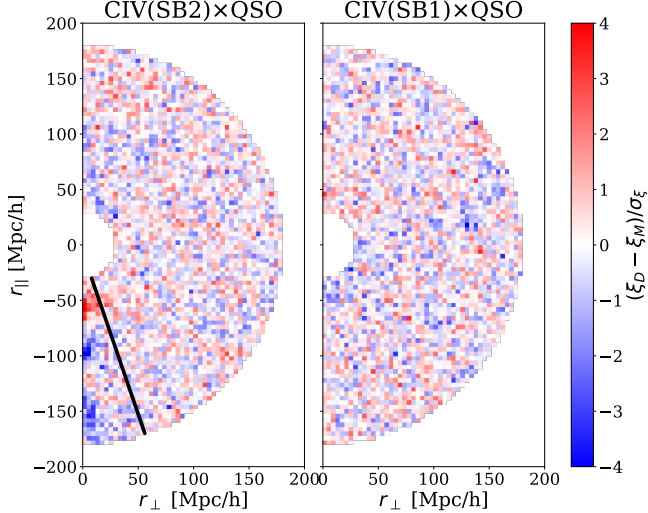


Figure 9. Residuals of the best-fit model for the baseline analysis with data for the CIV×QSO cross-correlation shown for each side band. The area to the left of the black line is the wedge ($-1.0 \leq \mu < -0.95$) excluded from the fit due to redshift errors, where the oscillations are clearly present. SB1 has no visible oscillations because they occur at $|r_{\parallel}| > 200 h^{-1}$ Mpc.

move this contamination. For quasar-pixel pairs in the cross-correlation, the contamination is strongest when the tracer quasar is closer to the host quasar of the forest. [Gordon et al. \(2023\)](#) and [Casas et al. \(2025\)](#) showed that removing close quasar-pixel pairs removes most of the spurious correlations and therefore reduces the small bias on α_{\parallel} . We remove close pairs by performing cuts in the correlations to remove pairs that are spatially close and that are close in redshift. Shown in Figure 10, removing the close pairs does not affect the results on α_{iso} .

With our exclusion of the wedge along the line of sight at negative r_{\parallel} in SB2 (between $-1.0 \leq \mu < -0.95$), we find that we have a good agreement between the data and the best-fit model.

The best fit for CIV(SB1)×ELG is very noisy. This is likely due to the CIV forest sample in SB1 having little to no overlap with the ELG tracer redshifts. The SiIV region is only visible in quasar spectra with $z > 1.6$ and the ELG redshifts used in this work are all at redshifts $z < 1.6$. Though it is included in this work, we recommend that any future studies should exclude the CIV(SB1)×ELG cross-correlation unless a better overlap in redshift is achieved.

4.3. Validation Tests

In this work, we follow the procedure for a well-developed method for measuring BAO with the Lyman- α forest. Though this method has been carefully tested and validated starting over a decade ago with SDSS,

there have been few studies using this procedure with an absorber other than the Lyman- α forest, and even fewer studies using CIV as an absorber. In fact, the latest measurement of BAO from the CIV forest comes from [Blomqvist et al. \(2018\)](#) which measured BAO from SDSS DR14, though they did not get a statistically significant detection. There have been no previous studies that cross-correlate ELGs with CIV flux fluctuations (absorption).

Given the much larger dataset of DESI DR2, any validation tests would normally be run on synthetic datasets, or mocks. Unfortunately, at the time of this paper, there were no synthetic CIV forest datasets available and we were unable to validate any of our results using mock datasets. Instead, we apply validation tests to the data.

We were able to apply a blinding scheme during all measurements and validation tests. Since this work was performed after the release of the [DESI-2025-I](#), we use a different blinding scheme than what was used in [DESI-2025-I](#). There, they applied a blinding scheme at the level of the correlations themselves. Because the pipeline no longer automatically blinded the correlations, in this work we instead apply our blinding scheme to the fits where we randomly shift the BAO parameters (α_{\parallel} , α_{\perp} , α_{iso}) by a pre-determined seeded amount. This is the same blinding scheme that was used in the DESI DR1 Lyman- α forest full-shape analysis ([Cuceu et al. 2025](#)). Only after obtaining and understanding the results from the validation tests were the baseline results unblinded. Our goal for unblinding was that any shifts to α_{iso} from the analysis variations would be less than $\frac{1}{3}\sigma_{\text{baseline}}$ and that all fits would be valid.

We run two types of validation tests on our analysis. The first is different analysis variations where we explore how various changes in the method affect the BAO results. These variations are discussed in section 4.3.1. The second is data splits, where the dataset is split into two based on some criteria. In this work, we only study one data split based on the equivalent width of the CIV line and we discuss the results in section 4.3.2.

4.3.1. Analysis Variations

We run the same analysis variations on both the quasar and ELG measurements and use the same fit parameters as in the baseline fit with small adjustments where appropriate. We present the results for the combined fits in Figure 10, which shows the one-dimensional shifts in α_{iso} for all analysis variations. The variations are grouped based on which part of the analysis is changed. The green point is a change to the dataset:

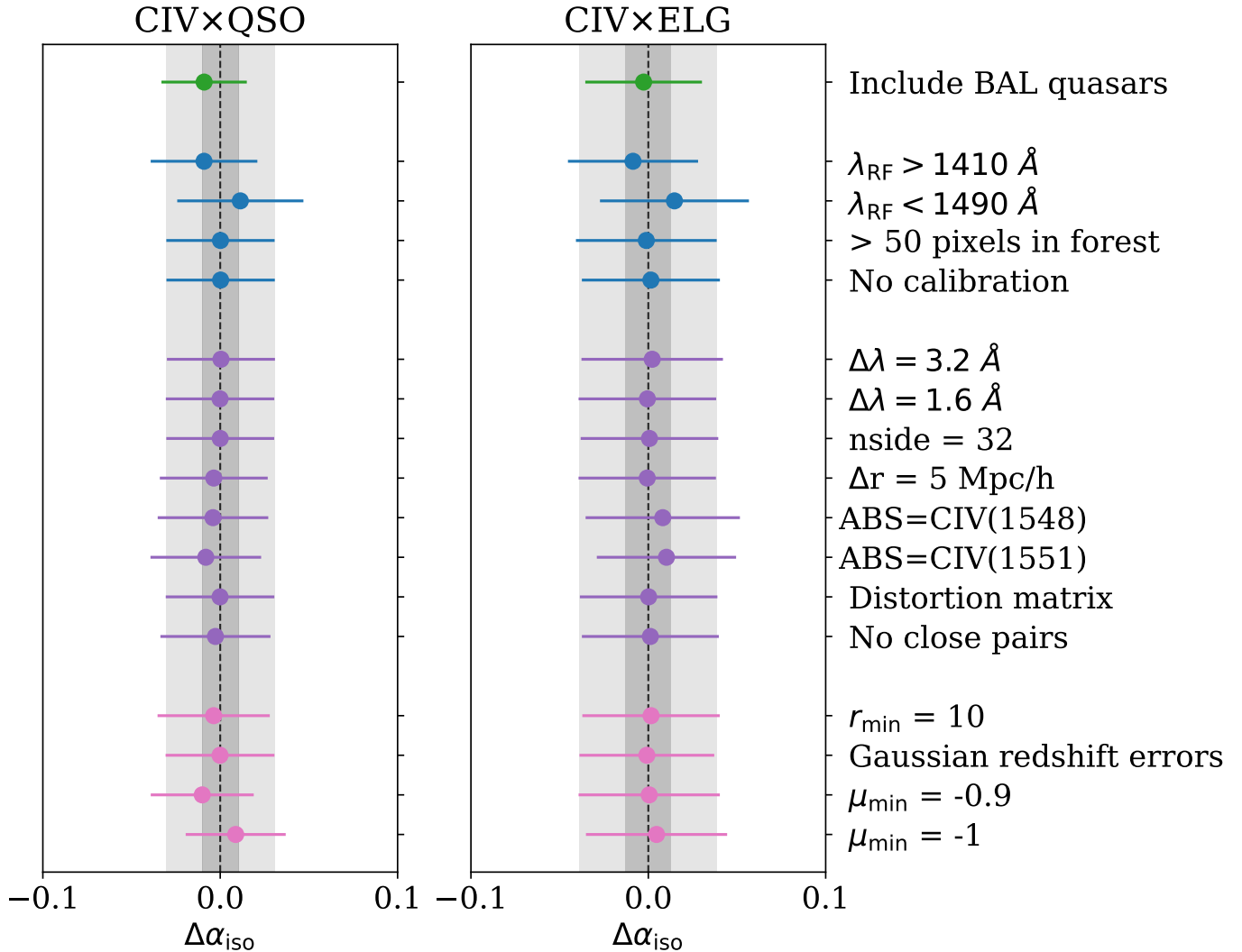


Figure 10. Shifts in the isotropic BAO parameter α_{iso} from the different analysis variations run. Each analysis variation changes one part of the analysis. The green point corresponds to changes to the dataset; the blue points correspond to changes to the continuum fitting method; the purple points correspond to changes in the calculation of the correlations; and the pink points correspond to changes in the fit. The dark and light grey regions correspond to $\frac{1}{3}\sigma_{\text{baseline}}$ and σ_{baseline} , respectively. All variations for both tracers are within the $\frac{1}{3}\sigma_{\text{baseline}}$ goal except for the “ $\lambda_{RF} < 1490 \text{ \AA}$ ” variation. This shift is within the expected statistical shift from using a subset of the baseline dataset.

- **include BAL quasars:** we use the quasar catalog from [DESI-2025-I](#) that includes BAL quasars. The BAL quasars are used as tracers and BAL regions are masked during the continuum fitting process following [Martini et al. \(2025\)](#);

the blue points are changes to the continuum fitting method:

- $\lambda_{RF} > 1410 \text{ \AA}$: we extend the length of the CIV region from 1420 \AA to 1410 \AA . The SiIV region remains the same as in baseline,
- $\lambda_{RF} < 1490 \text{ \AA}$: we shorten the length of the CIV region from 1520 \AA to 1490 \AA . The SiIV region remains the same as in baseline,

- >50 pixels in forest: we include lines-of-sight in both forest regions with more than 50 valid forest pixels. For the baseline analysis we required at least 90 pixels in SB2 and 110 pixels in SB1,

- no calibration: we do not perform the recalibration step described in [Ramírez-Pérez et al. \(2024\)](#);

the purple points are changes to the correlation calculation:

- $\Delta\lambda = 3.2 \text{ \AA}$: we re-bin both forest samples by 4 pixels rather than by 3 pixels ($\Delta\lambda = 2.4 \text{ \AA}$),

- $\Delta\lambda = 1.6\text{\AA}$: we re-bin both forest samples by 2 pixels rather than by 3 pixels,
- $nside = 32$: we measure the correlations in HEALPix pixels with $nside=32$ rather than $nside=16$ as in the baseline analysis,
- $\Delta r = 5 \text{ Mpc/h}$: we use a $5 h^{-1}$ Mpc binning of the correlations and distortion matrices rather than the $4 h^{-1}$ Mpc binning in baseline,
- **ABS=CIV(1548)**: we use the $\lambda_{RF} = 1548.20\text{\AA}$ line of the doublet as the absorber instead of the average wavelength,
- **ABS=CIV(1551)**: we use the $\lambda_{RF} = 1551.78\text{\AA}$ line of the doublet as the absorber instead of the average wavelength,
- **distortion matrix**: we change the percent of the dataset used to calculate the distortion matrix. For the quasar measurement we use 2% of the dataset rather than 1%. For the ELG measurement we use 0.5% of the dataset rather than 0.1%,
- **no close pairs**: we remove quasar-pixel (or ELG-pixel) pairs that could potentially contaminate the correlations on small-scales. We use an extreme cut of 0.33 degrees and 10,000 km/s. This cut is applied to pairs in the correlations and distortion matrices;

and the pink points are changes to the fit:

- $r_{\min} = 10$: we change the minimum distance in the fit from $30 h^{-1}$ Mpc to $10 h^{-1}$ Mpc,
- **Gaussian redshift errors**: we model quasar redshift errors with a Gaussian model rather than the Lorentzian model used in the baseline analysis,
- $\mu_{\min} = -0.9$: we change the angular wedge used in the fit from -0.95 to -0.9 to restrict the μ range further,
- $\mu_{\min} = -1.0$: we change the angular wedge used in the fit from -0.95 to -1.0 to allow the full μ range.

The dark and light grey regions in Figure 10 correspond to $\frac{1}{3}\sigma_{\text{baseline}}$ and σ_{baseline} , respectively.

For the variations where we choose one line of the doublet as the absorber (**ABS=CIV(1548)** and **ABS=CIV(1551)**), we add an additional free parameter to the fit (either $b_{\text{CIV}(1551)}$ or $b_{\text{CIV}(1548)}$, respectively)

to model the other line of the doublet as a metal contaminant. To preserve the extracted BAO information, we also need to include the BAO model for the cross-correlation with the line of the doublet that is treated as a metal contaminant.

For both the quasar and ELG measurements, all but one of the variations are within $\frac{1}{3}\sigma_{\text{baseline}}$ and the error-bars are of similar magnitude to the baseline fit. The variation that does not meet the goal is $\lambda_{RF} < 1490 \text{ \AA}$ and the shifts to α_{iso} are 0.011 for quasars and 0.014 for ELGs. This variation uses a subset of the baseline analysis by restricting the length of the CIV region. We can calculate the expected statistical shift for each measurement and find that it is around 0.04 for both tracers, showing that this shift is within the expected statistical fluctuation.

4.3.2. Data Splits

We study the effects on our BAO results when splitting our quasar catalog into two based on the equivalent width (EW) of the CIV doublet. A similar analysis was performed in [Adame et al. \(2025b\)](#). This split is motivated by the Baldwin Effect ([Baldwin 1977](#)), which is the anti-correlation between the EW of quasar emission lines and the luminosity of the continuum. Due to this, we expect the shape of the quasar spectral energy distribution (SED) to depend on the CIV EW.

The equivalent width information was taken from the **FastSpecFit**³ ([Moustakas et al. 2023](#)) catalogs and added to our quasar catalog. The quasar catalog is then split at the median equivalent width of 48 \AA . We again remove all BAL quasars.

The results on α_{iso} for the two data splits are:

$$\begin{aligned} \alpha_{\text{iso}} &= 1.081 \pm 0.190 \text{ (CIV} > 48\text{\AA}) \\ \alpha_{\text{iso}} &= 1.142 \pm 0.054 \text{ (CIV} < 48\text{\AA}) \end{aligned} \quad (11)$$

These results are consistent with each other and with the combined quasar result. The errorbars of the data splits did increase compared to the main result, but this is not unexpected, as this data split cuts a measurement that was already not very strong into two even weaker measurements.

4.4. Cosmology Results

Figure 11 shows how the BAO measurements from this work compare to the results and best-fit ΛCDM model from [DESI-2025-II](#) and from [Planck Collaboration et al. \(2020\)](#). The BAO measurements are

³ **FastSpecFit** is a stellar continuum and emission-line modeling code designed to model DESI data. More information can be found at <https://fastspecfit.readthedocs.io/>.

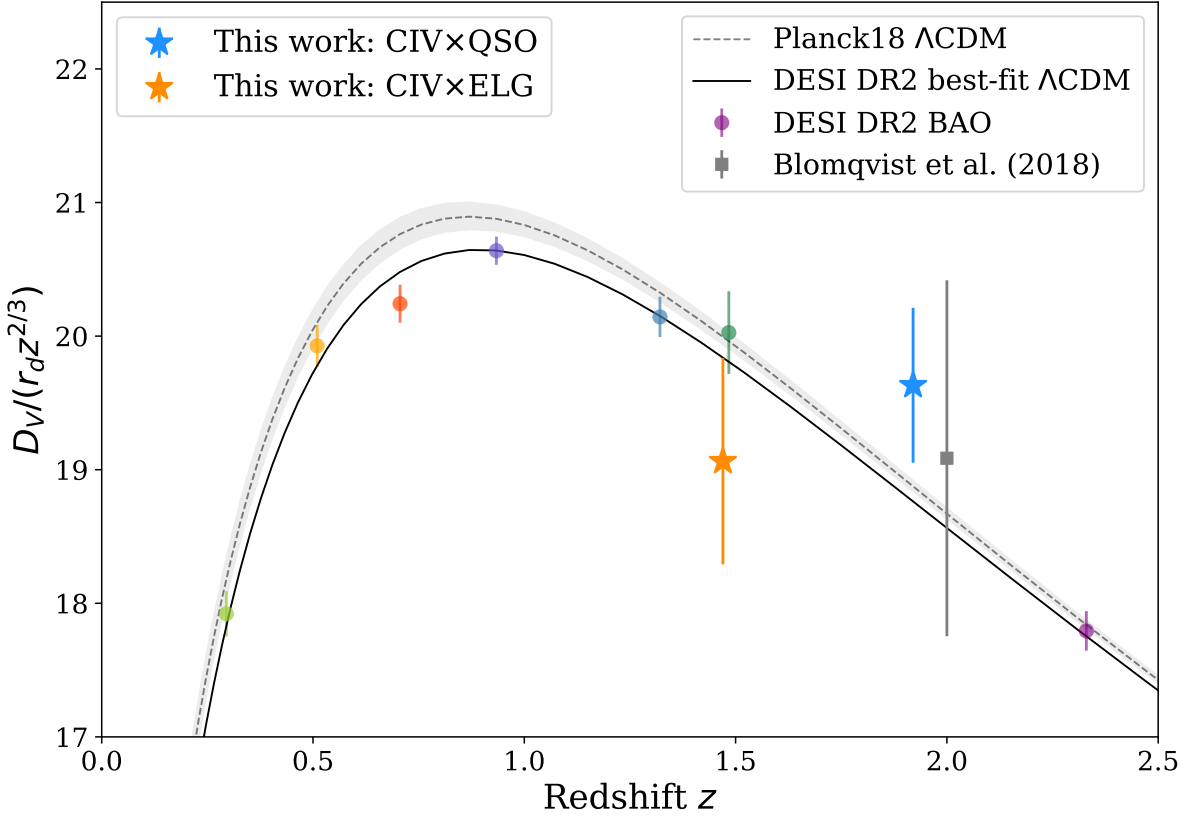


Figure 11. Measurements of the BAO distance parametrized as the ratio of the angle-averaged distance D_V and the sound horizon r_d . We apply a scaling of $z^{-2/3}$ for visualization purposes. The measurement from the combined fit with quasars from this work is shown as the blue star at $z_{\text{eff}} = 1.92$. We show the measurement from the combined fit with ELGs for completeness as the orange star. The measurements from the various tracers from [DESI-2025-II](#) are shown as the multi-colored points (from left to right: BGS, LRG, LRG, LRG+ELG, ELG, QSO, LY α). The solid black line is the best-fit Λ CDM model from [DESI-2025-II](#) and the dashed grey line is the Λ CDM model from [Planck Collaboration et al. \(2020\)](#). The grey square shows the result from [Blomqvist et al. \(2018\)](#).

parametrized as the ratio of the angle-averaged distance D_V (from equation 7) to the sound horizon at the baryon drag epoch, r_d . For the combined fit with quasars, we find

$$D_V/r_d(z_{\text{eff}} = 1.92) = 30.3 \pm 0.9, \quad (12)$$

shown as the blue star in Figure 11, is statistically consistent with the best fit Λ CDM results from [DESI-2025-II](#).

We present the measurement with ELGs (orange star in Figure 11) for completeness and we find

$$D_V/r_d(z_{\text{eff}} = 1.47) = 24.6 \pm 1.0. \quad (13)$$

The values shown in Figure 11 are scaled by $z^{-2/3}$ for visualization purposes.

5. SUMMARY

We present the first DESI measurement of BAO using cross-correlations of the C IV forest fluctuations with quasars and a proof of concept measurement of the cross-correlation of the C IV forest with ELGs. These measurements are based on the first three years of DESI main survey data which will be released with data release 2 (DR2).

We find a 4.2σ detection of BAO from the C IV \times QSO cross-correlation and a corresponding uncertainty on α_{iso} of 3.1% at an effective redshift $z_{\text{eff}} = 1.92$. We find a corresponding isotropic distance measurement of $D_V/r_d = 30.3 \pm 0.9$.

We measure the BAO signal at 2.5σ significance in the C IV \times ELG cross-correlation. The uncertainty on α_{iso} is

4% at an effective redshift of $z_{\text{eff}} = 1.47$. The isotropic distance measurement is $D_V/r_d = 24.6 \pm 1.0$.

We validated our measurements by performing several analysis variations for both tracers to test how small changes to the method affect the result on α_{iso} . We set a goal that $\Delta\alpha_{\text{iso}} < \frac{1}{3}\sigma_{\text{baseline}}$ and all but one of the variations met this goal. This variation used a subset of the baseline dataset by shortening the length of the C IV region (changing the limit from 1520 Å to 1490 Å). We confirmed that the larger shift was within the expected statistical fluctuation for this smaller dataset. We also performed one data split based on the equivalent width of the C IV line. The two splits were in agreement with each other and with the baseline quasar result. We did not perform this data split on the ELG measurement.

Future work will look to improve the uncertainty on the C IV \times QSO cross-correlation and increase the significance of the C IV \times ELG cross-correlation detection. The main way to do this is by increasing the signal in the C IV and Si IV regions of quasar spectra which, in turn, will increase the signal in the C IV forest samples. For Lyman- α studies, this is achieved by observing quasars ($z > 2.1$) multiple times. In DESI DR2, only 15.8% of quasars between $1.4 < z < 2.1$ were observed more than once, shrinking to just 3.4% for those observed more than twice. We estimate that we can reduce our error on α_{iso} by a factor of two by observing low-redshift quasars ($1.4 < z < 2.1$) four times.

One immediate improvement on the uncertainty could be obtained by including BAL quasars. BALs are more likely to be identified in spectra with a higher signal-to-noise ratio (SNR). By excluding the BAL quasars from our C IV forest samples, we discarded spectra that had higher signal in the C IV and Si IV regions. Our validation test where we included BAL quasars confirms that we can improve the uncertainty on α_{iso} by including these quasars. When including BALs, the error on α_{iso} for the C IV \times QSO measurement is only 2.4% and nearly 3.2% for the ELG \times QSO measurement. This validation test was performed with the BAL masking strategy described in Martini et al. (2025), but future studies could decide if there are any improvements to be made.

There are many future studies that could be conducted on how the C IV forest samples are obtained. In this work, we used `picca` to obtain the unabsorbed continuum in the C IV and Si IV regions. `picca` was designed to measure the continuum in the Lyman- α region, where the absorption due to Lyman- α is incredibly dense. Given that the C IV absorption in the C IV and Si IV regions is significantly less dense, one could look into other methods (such as spline fitting (Pieri 2014)) to estimate the continuum. Another continuum

prediction one could use is LyCAN, a convolutional neural network that predicts the unabsorbed quasar continuum within the rest-frame wavelength range of 1040 Å to 1600 Å (Turner et al. 2024). Other studies could look at whether or not C IV absorption could be extracted from ELG spectra, and if so, whether combining these forests with the forest samples in this work could help improve the uncertainty on α_{iso} .

We leave these studies as potential future work, but reiterate that with improvements to the uncertainties, this work has the potential to provide a key BAO measurement for DESI at an effective redshift that the current tracers do not cover.

DATA AVAILABILITY

The data used in this analysis will be made public along with Data Release 2 (<https://data.desi.lbl.gov/doc/releases/>). The data points for reproducing figures will be made available on Zenodo upon journal publication.

ACKNOWLEDGMENTS

AC acknowledges support provided by NASA through the NASA Hubble Fellowship grant HST-HF2-51526.001-A awarded by the Space Telescope Science Institute, which is operated by the Association of Universities for Research in Astronomy, Incorporated, under NASA contract NAS5-26555.

This material is based upon work supported by the U.S. Department of Energy (DOE), Office of Science, Office of High-Energy Physics, under Contract No. DE-AC02-05CH11231, and by the National Energy Research Scientific Computing Center, a DOE Office of Science User Facility under the same contract. Additional support for DESI was provided by the U.S. National Science Foundation (NSF), Division of Astronomical Sciences under Contract No. AST-0950945 to the NSF's National Optical-Infrared Astronomy Research Laboratory; the Science and Technology Facilities Council of the United Kingdom; the Gordon and Betty Moore Foundation; the Heising-Simons Foundation; the French Alternative Energies and Atomic Energy Commission (CEA); the National Council of Humanities, Science and Technology of Mexico (CONAH-CYT); the Ministry of Science, Innovation and Universities of Spain (MICIU/AEI/10.13039/501100011033), and by the DESI Member Institutions: <https://www.desi.lbl.gov/collaborating-institutions>. Any opinions, findings, and conclusions or recommendations expressed in this material are those of the author(s) and do not necessarily reflect the views of the U. S. National Science Foundation, the U. S. Department of Energy, or any of the listed funding agencies.

The authors are honored to be permitted to conduct scientific research on I'oligam Du'ag (Kitt Peak),

a mountain with particular significance to the Tohono O'odham Nation.

REFERENCES

- Abolfathi, B., Aguado, D. S., Aguilar, G., et al. 2018, *ApJS*, 235, 42, doi: [10.3847/1538-4365/aa9e8a](https://doi.org/10.3847/1538-4365/aa9e8a)
- Adame, A. G., Aguilar, J., Ahlen, S., et al. 2025a, *JCAP*, 2025, 012, doi: [10.1088/1475-7516/2025/04/012](https://doi.org/10.1088/1475-7516/2025/04/012)
- . 2025b, *JCAP*, 2025, 124, doi: [10.1088/1475-7516/2025/01/124](https://doi.org/10.1088/1475-7516/2025/01/124)
- . 2025c, *JCAP*, 2025, 028, doi: [10.1088/1475-7516/2025/07/028](https://doi.org/10.1088/1475-7516/2025/07/028)
- . 2025d, *JCAP*, 2025, 021, doi: [10.1088/1475-7516/2025/02/021](https://doi.org/10.1088/1475-7516/2025/02/021)
- Alam, S., Albareti, F. D., Allende Prieto, C., et al. 2015, *ApJS*, 219, 12, doi: [10.1088/0067-0049/219/1/12](https://doi.org/10.1088/0067-0049/219/1/12)
- Anand, A., Nelson, D., & Kauffmann, G. 2021, *MNRAS*, 504, 65, doi: [10.1093/mnras/stab871](https://doi.org/10.1093/mnras/stab871)
- Anand, A., Aguilar, J., Ahlen, S., et al. 2025, arXiv e-prints, arXiv:2504.20299, doi: [10.48550/arXiv.2504.20299](https://doi.org/10.48550/arXiv.2504.20299)
- Bailey, S. 2025, *in preparation*
- Baldwin, J. A. 1977, *ApJ*, 214, 679, doi: [10.1086/155294](https://doi.org/10.1086/155294)
- Bault, A., Kirkby, D., Guy, J., et al. 2025, *JCAP*, 2025, 130, doi: [10.1088/1475-7516/2025/01/130](https://doi.org/10.1088/1475-7516/2025/01/130)
- Bautista, J. E., Busca, N. G., Guy, J., et al. 2017, *A&A*, 603, A12, doi: [10.1051/0004-6361/201730533](https://doi.org/10.1051/0004-6361/201730533)
- Blomqvist, M., Pieri, M. M., du Mas des Bourboux, H., et al. 2018, *JCAP*, 2018, 029, doi: [10.1088/1475-7516/2018/05/029](https://doi.org/10.1088/1475-7516/2018/05/029)
- Brodzeller, A., Dawson, K., Bailey, S., et al. 2023, *AJ*, 166, 66, doi: [10.3847/1538-3881/ace35d](https://doi.org/10.3847/1538-3881/ace35d)
- Busca, N. G., & Balland, C. 2021, QuasarNET: CNN for redshifting and classification of astrophysical spectra, *Astrophysics Source Code Library*, record ascl:2106.016, <http://ascl.net/2106.016>
- Casas, L., Herrera-Alcantar, H. K., Chaves-Montero, J., et al. 2025, arXiv e-prints, arXiv:2503.14741, doi: [10.48550/arXiv.2503.14741](https://doi.org/10.48550/arXiv.2503.14741)
- Chaussidon, E., Yèche, C., Palanque-Delabrouille, N., et al. 2023, *ApJ*, 944, 107, doi: [10.3847/1538-4357/abc3c2](https://doi.org/10.3847/1538-4357/abc3c2)
- Chaussidon, E., Yèche, C., de Mattia, A., et al. 2025, *JCAP*, 2025, 029, doi: [10.1088/1475-7516/2025/06/029](https://doi.org/10.1088/1475-7516/2025/06/029)
- Cooksey, K. L., Kao, M. M., Simcoe, R. A., O'Meara, J. M., & Prochaska, J. X. 2013, *ApJ*, 763, 37, doi: [10.1088/0004-637X/763/1/37](https://doi.org/10.1088/0004-637X/763/1/37)
- Cuceu, A., Font-Ribera, A., Martini, P., et al. 2023, *MNRAS*, 523, 3773, doi: [10.1093/mnras/stad1546](https://doi.org/10.1093/mnras/stad1546)
- Cuceu, A., Herrera-Alcantar, H. K., Gordon, C., et al. 2025, arXiv e-prints, arXiv:2509.15308, doi: [10.48550/arXiv.2509.15308](https://doi.org/10.48550/arXiv.2509.15308)
- de Belsunce, R., Chen, S.-F., Ivanov, M. M., et al. 2025, *PhRvD*, 111, 063524, doi: [10.1103/PhysRevD.111.063524](https://doi.org/10.1103/PhysRevD.111.063524)
- DESI Collaboration, Aghamousa, A., Aguilar, J., et al. 2016, arXiv e-prints, arXiv:1611.00037, doi: [10.48550/arXiv.1611.00037](https://doi.org/10.48550/arXiv.1611.00037)
- DESI Collaboration, Abareshi, B., Aguilar, J., et al. 2022, *AJ*, 164, 207, doi: [10.3847/1538-3881/ac882b](https://doi.org/10.3847/1538-3881/ac882b)
- DESI Collaboration, Adame, A. G., Aguilar, J., et al. 2024, *AJ*, 168, 58, doi: [10.3847/1538-3881/ad3217](https://doi.org/10.3847/1538-3881/ad3217)
- DESI Collaboration, Abdul-Karim, M., Adame, A. G., et al. 2025a, arXiv e-prints, arXiv:2503.14745, doi: [10.48550/arXiv.2503.14745](https://doi.org/10.48550/arXiv.2503.14745)
- DESI Collaboration, Abdul-Karim, M., Aguilar, J., et al. 2025b, arXiv e-prints, arXiv:2503.14739, doi: [10.48550/arXiv.2503.14739](https://doi.org/10.48550/arXiv.2503.14739)
- . 2025c, arXiv e-prints, arXiv:2503.14738, doi: [10.48550/arXiv.2503.14738](https://doi.org/10.48550/arXiv.2503.14738)
- du Mas des Bourboux, H., Dawson, K. S., Busca, N. G., et al. 2019, *ApJ*, 878, 47, doi: [10.3847/1538-4357/ab1d49](https://doi.org/10.3847/1538-4357/ab1d49)
- du Mas des Bourboux, H., Rich, J., Font-Ribera, A., et al. 2020, *ApJ*, 901, 153, doi: [10.3847/1538-4357/abb085](https://doi.org/10.3847/1538-4357/abb085)
- . 2021, picca: Package for IgM Cosmological-Correlations Analyses, *Astrophysics Source Code Library*, record ascl:2106.018, <http://ascl.net/2106.018>
- Eisenstein, D. J., & Bennett, C. L. 2008, *Physics Today*, 61, 44, doi: [10.1063/1.2911177](https://doi.org/10.1063/1.2911177)
- Eisenstein, D. J., & Hu, W. 1998, *ApJ*, 496, 605, doi: [10.1086/305424](https://doi.org/10.1086/305424)
- Eisenstein, D. J., Seo, H.-J., & White, M. 2007, *ApJ*, 664, 660, doi: [10.1086/518755](https://doi.org/10.1086/518755)
- Ennesser, L., Martini, P., Font-Ribera, A., & Pérez-Ràfols, I. 2022, *MNRAS*, 511, 3514, doi: [10.1093/mnras/stac301](https://doi.org/10.1093/mnras/stac301)
- Ferraro, S., Sailer, N., Slosar, A., & White, M. 2022, arXiv e-prints, arXiv:2203.07506, doi: [10.48550/arXiv.2203.07506](https://doi.org/10.48550/arXiv.2203.07506)
- Filbert, S., Martini, P., Seebaluck, K., et al. 2024, *MNRAS*, 532, 3669, doi: [10.1093/mnras/stae1610](https://doi.org/10.1093/mnras/stae1610)
- Font-Ribera, A., & Miralda-Escudé, J. 2012, *JCAP*, 2012, 028, doi: [10.1088/1475-7516/2012/07/028](https://doi.org/10.1088/1475-7516/2012/07/028)
- Gontcho A Gontcho, S., Miralda-Escudé, J., Font-Ribera, A., et al. 2018, *MNRAS*, 480, 610, doi: [10.1093/mnras/sty1817](https://doi.org/10.1093/mnras/sty1817)

- Gordon, C., Cuceu, A., Chaves-Montero, J., et al. 2023, *JCAP*, 2023, 045, doi: [10.1088/1475-7516/2023/11/045](https://doi.org/10.1088/1475-7516/2023/11/045)
- Gordon, C., Cuceu, A., Font-Ribera, A., et al. 2025, arXiv e-prints, arXiv:2505.08789, doi: [10.48550/arXiv.2505.08789](https://doi.org/10.48550/arXiv.2505.08789)
- Green, D., Kirkby, D., Aguilar, J., et al. 2025, *JCAP*, 2025, 087, doi: [10.1088/1475-7516/2025/10/087](https://doi.org/10.1088/1475-7516/2025/10/087)
- Guo, Z., & Martini, P. 2019, *ApJ*, 879, 72, doi: [10.3847/1538-4357/ab2590](https://doi.org/10.3847/1538-4357/ab2590)
- Guy, J., Bailey, S., Kremin, A., et al. 2023, *AJ*, 165, 144, doi: [10.3847/1538-3881/acb212](https://doi.org/10.3847/1538-3881/acb212)
- Guy, J., Gontcho, S. G. A., Armengaud, E., et al. 2025, *JCAP*, 2025, 140, doi: [10.1088/1475-7516/2025/01/140](https://doi.org/10.1088/1475-7516/2025/01/140)
- Hadzhiyska, B., de Belsunce, R., Cuceu, A., et al. 2025, *MNRAS*, 540, 1960, doi: [10.1093/mnras/staf824](https://doi.org/10.1093/mnras/staf824)
- Herrera-Alcantar, H. K., Armengaud, E., Yèche, C., et al. 2025, arXiv e-prints, arXiv:2507.21852, doi: [10.48550/arXiv.2507.21852](https://doi.org/10.48550/arXiv.2507.21852)
- Hu, W., & Sugiyama, N. 1996, *ApJ*, 471, 542, doi: [10.1086/177989](https://doi.org/10.1086/177989)
- Martini, P., Cuceu, A., Ennesser, L., et al. 2025, *JCAP*, 2025, 137, doi: [10.1088/1475-7516/2025/01/137](https://doi.org/10.1088/1475-7516/2025/01/137)
- McDonald, P., Seljak, U., Burles, S., et al. 2006, *ApJS*, 163, 80, doi: [10.1086/444361](https://doi.org/10.1086/444361)
- Miller, T. N., Doel, P., Gutierrez, G., et al. 2024, *AJ*, 168, 95, doi: [10.3847/1538-3881/ad45fe](https://doi.org/10.3847/1538-3881/ad45fe)
- Moustakas, J., Buhler, J., Scholte, D., Dey, B., & Khederlarian, A. 2023, FastSpecFit: Fast spectral synthesis and emission-line fitting of DESI spectra, *Astrophysics Source Code Library*, record ascl:2308.005. <http://ascl.net/2308.005>
- Napolitano, L., Pandey, A., Myers, A. D., et al. 2023, *AJ*, 166, 99, doi: [10.3847/1538-3881/ace62c](https://doi.org/10.3847/1538-3881/ace62c)
- Ouchi, M., Ono, Y., & Shibuya, T. 2020, *ARA&A*, 58, 617, doi: [10.1146/annurev-astro-032620-021859](https://doi.org/10.1146/annurev-astro-032620-021859)
- Pieri, M. M. 2014, *MNRAS*, 445, L104, doi: [10.1093/mnrasl/sl4142](https://doi.org/10.1093/mnrasl/sl4142)
- Pieri, M. M., Mortonson, M. J., Frank, S., et al. 2014, *MNRAS*, 441, 1718, doi: [10.1093/mnras/stu577](https://doi.org/10.1093/mnras/stu577)
- Planck Collaboration, Aghanim, N., Akrami, Y., et al. 2020, *A&A*, 641, A6, doi: [10.1051/0004-6361/201833910](https://doi.org/10.1051/0004-6361/201833910)
- Poppett, C., Tyas, L., Aguilar, J., et al. 2024, *AJ*, 168, 245, doi: [10.3847/1538-3881/ad76a4](https://doi.org/10.3847/1538-3881/ad76a4)
- Raichoor, A., Moustakas, J., Newman, J. A., et al. 2023, *AJ*, 165, 126, doi: [10.3847/1538-3881/acb213](https://doi.org/10.3847/1538-3881/acb213)
- Ramírez-Pérez, C., Pérez-Ràfols, I., Font-Ribera, A., et al. 2024, *MNRAS*, 528, 6666, doi: [10.1093/mnras/stad3781](https://doi.org/10.1093/mnras/stad3781)
- Ross, A. J., Aguilar, J., Ahlen, S., et al. 2025, *JCAP*, 2025, 125, doi: [10.1088/1475-7516/2025/01/125](https://doi.org/10.1088/1475-7516/2025/01/125)
- Sailer, N., Castorina, E., Ferraro, S., & White, M. 2021, *JCAP*, 2021, 049, doi: [10.1088/1475-7516/2021/12/049](https://doi.org/10.1088/1475-7516/2021/12/049)
- Schlafly, E. F., Kirkby, D., Schlegel, D. J., et al. 2023, *AJ*, 166, 259, doi: [10.3847/1538-3881/ad0832](https://doi.org/10.3847/1538-3881/ad0832)
- Shen, Y., Brandt, W. N., Richards, G. T., et al. 2016, *ApJ*, 831, 7, doi: [10.3847/0004-637X/831/1/7](https://doi.org/10.3847/0004-637X/831/1/7)
- Silber, J. H., Fagrelius, P., Fanning, K., et al. 2023, *AJ*, 165, 9, doi: [10.3847/1538-3881/ac9ab1](https://doi.org/10.3847/1538-3881/ac9ab1)
- Turner, W., Martini, P., Karaçaylı, N. G., et al. 2024, *ApJ*, 976, 143, doi: [10.3847/1538-4357/ad8239](https://doi.org/10.3847/1538-4357/ad8239)
- Weinberg, D. H., Mortonson, M. J., Eisenstein, D. J., et al. 2013, *PhR*, 530, 87, doi: [10.1016/j.physrep.2013.05.001](https://doi.org/10.1016/j.physrep.2013.05.001)
- White, M., Raichoor, A., Dey, A., et al. 2024, *JCAP*, 2024, 020, doi: [10.1088/1475-7516/2024/08/020](https://doi.org/10.1088/1475-7516/2024/08/020)
- Yang, L., Zheng, Z., du Mas des Bourboux, H., et al. 2022, *ApJ*, 935, 121, doi: [10.3847/1538-4357/ac7b2e](https://doi.org/10.3847/1538-4357/ac7b2e)
- Youles, S., Bautista, J. E., Font-Ribera, A., et al. 2022, *MNRAS*, 516, 421, doi: [10.1093/mnras/stac2102](https://doi.org/10.1093/mnras/stac2102)

APPENDIX

A. BASELINE FIT RESULTS

We show contour plots from our baseline fit from running the Polychord sampler on our correlations in Figures 12 and 13. Figure 12 shows the results from the combined fit with quasars (black line contours), as well as fits to the individual side bands (purple and blue contours). Figure 13 shows the analogous results for ELGs. The contours from the three fits for each tracer are in good agreement.

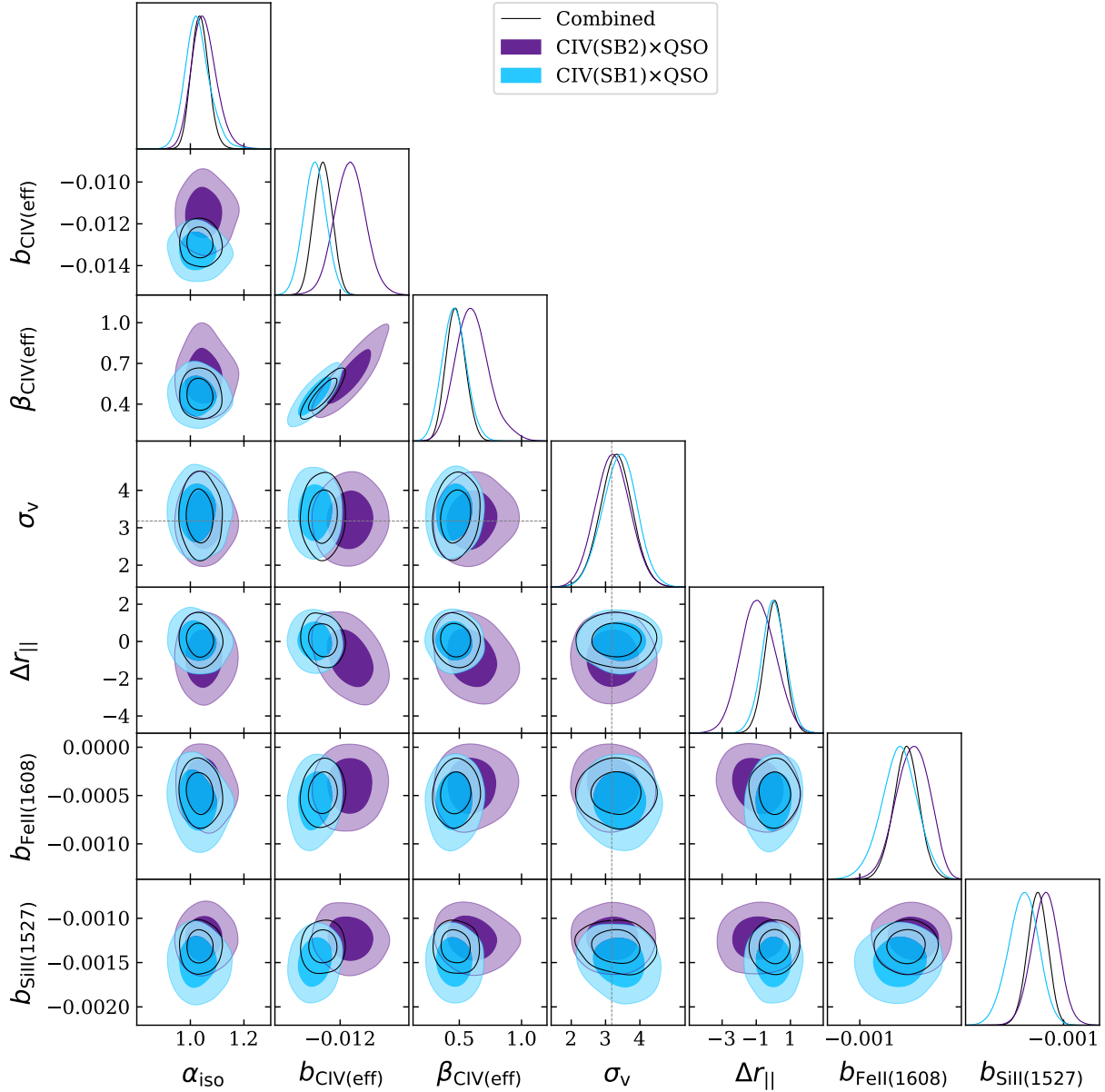


Figure 12. Results from running the sampler on the CIV(SB2) \times QSO (purple), CIV(SB1) \times QSO (blue), and combined (black) fits.

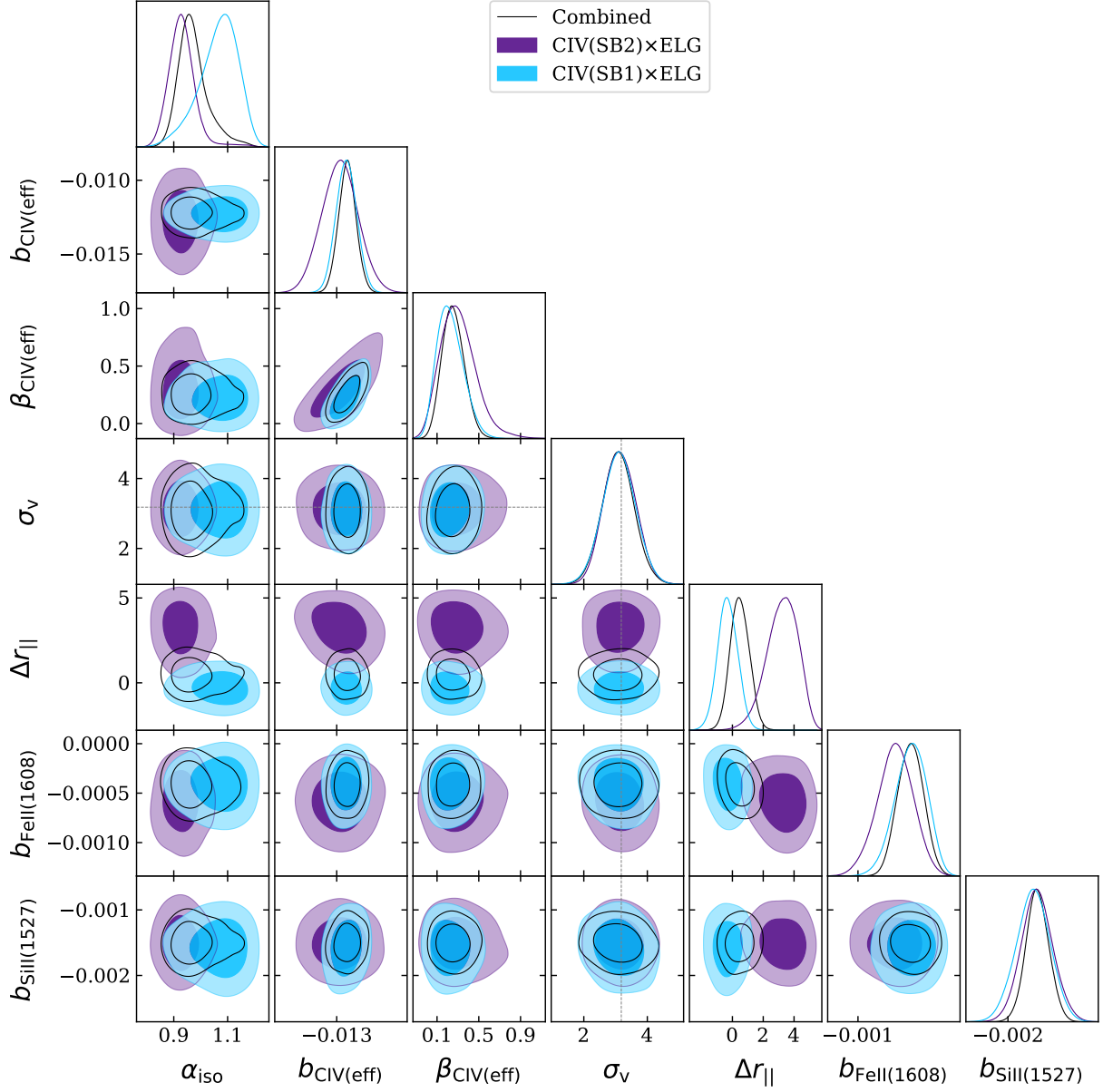


Figure 13. Results from running the sampler on the CIV(SB2) \times ELG (purple), CIV(SB1) \times ELG (blue), and combined (black) fits.